ACS APPLIED MATERIALS & INTERFACES

Research Article

www.acsami.org

Low-Cost Copper Nanostructures Impart High Efficiencies to Quantum Dot Solar Cells

P. Naresh Kumar,[†] Melepurath Deepa,*[,†] and Partha Ghosal[‡]

[†]Department of Chemistry, Indian Institute of Technology Hyderabad, Ordnance Factory Estate, Yeddumailaram-502205, Telangana, India

[‡]Defence Metallurgical Research Laboratory, Defence Research & Development Organisation (DRDO), Hyderabad-500058, Telangana, India

Supporting Information

ABSTRACT: Quantum dot solar cells (QDSCs) were fabricated using low-cost Cu nanostructures and a carbon fabric as a counter electrode for the first time. Cu nanoparticles (NPs) and nanoneedles (NNs) with a face-centered cubic structure were synthesized by a hydrothermal method and electrophoretically deposited over a CdS QD sensitized titania (TiO_2) electrode. Compared to Cu NPs, which increase the light absorption of a TiO_2/CdS photoanode via scattering effects only in the visible region, Cu NNs are more effective for efficient far-field light scattering; they enhance the light absorption of the TiO_2/CdS assembly beyond the visible to near-infrared (NIR) regions as well. The highest fluorescence quenching, lowest excited electron lifetime, and a large surface potential (deduced from Kelvin probe force microscopy (KPFM)) observed for the TiO_2/CdS/Cu NN electrode compared to TiO_2/CdS and TiO_2/CdS/Cu NP electrodes confirm that Cu NNs also facilitate charge transport. KPFM studies also revealed a larger shift of the apparent Fermi level to more negative potentials in the TiO_2/CdS/Cu NN electrode, compared to the other two electrodes (versus NHE), which results in a higher open-circuit voltage for the Cu NN based electrode. The best performing QDSC based on the TiO_2/CdS/Cu NN electrode delivers a stellar power conversion efficiency (PCE) of 4.36%, greater by 56.8% and 32.1% than the PCEs produced by the cells based on TiO_2/CdS and TiO_2/CdS/Cu NPs, respectively. A maximum external quantum efficiency (EQE) of 58% obtained for the cell with the TiO_2/CdS/Cu NN electrode and a finite EQE in the NIR region which the other two cells do not deliver are clear indicators of the enormous promise this cheap, earth-abundant Cu nanostructure holds for amplifying the solar cell response in both the visible and near-infrared regions through scattering enhancements.

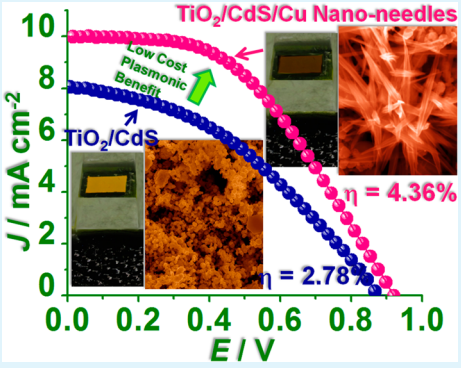

KEYWORDS: *quantum dots, solar cell, nanoparticles, nanoneedles, scattering*

INTRODUCTION

Among the newest approaches currently being used in third-generation solar cells such as dye-sensitized solar cells (DSSCs) for realizing significant improvements in net power conversion efficiencies (PCEs) is the use of noble-metal nanostructures. In this strategy, noble-metal (Ag or Au) nanostructures (nanowires/rods/particles, etc.) are embedded in photoanodes, typically composed of narrow band dye (such as N719 dye) molecules flanked to a wide band gap semiconductor (e.g., TiO_2).[1] The dye molecules usually absorb in the 400−600 nm wavelength range, and upon including a metal nanostructure in the assembly, the following phenomena are possible: (1) The absorption of dye molecules can increase via near-field electric field enhancement, upon surface plasmon excitation of the noble-metal nanostructures and their coupling with the dye molecules, (2) these nanostructures can also increase the light absorption capability of the photoanode via scattering, which rechannels light into the semiconductor and increases the optical path length of light, and (3) these metal nanostructures can be directly employed to harvest light and inject photogenerated electrons into an electron acceptor.[2] While there has been considerable progress in using plasmonic metal nanostructures in the photoanode in DSSCs, research on integrating metal nanomoieties into quantum dot solar cells (QDSCs) is very much in its infancy. Some milestones in this area pertaining to plasmonic DSSCs are summarized here.

In an earlier study, Qi et al. observed that the localized surface plasmons (LSPs) from Ag nanoparticles (NPs) increased the absorption of the dye molecules, which allowed them to decrease the thickness of the photoanodes, which in turn improved electron collection and device performance. With 0.6 wt % Ag@TiO_2 NPs, the efficiency of DSSCs with thin photoanodes (1.5 μm) increased from 3.1% to 4.4%. It was found that the plasmon-enhanced DSSCs required 62% less material to maintain the same efficiency as conventional DSSCs.[3] Core/shell/shell Au@SiO_2@TiO_2 nanostructures

Received: February 6, 2015
Accepted: May 22, 2015
Published: May 22, 2015

DOI: 10.1021/acsami.5b01175
ACS Appl. Mater. Interfaces 2015, 7, 13303−13313

were prepared, and the authors showed that when aggregates of nanoparticles were used, a very high efficiency DSSC (6.42%) was obtained.[4] In another investigation, by employing SiO_2- and TiO_2-capped Au nanoparticles, the efficiency of a N719 dye-sensitized solar cell (9.3%) increased to 10.2% upon incorporation of 0.7% Au@SiO_2 and to 9.8% upon loading of 0.7% Au@TiO_2 nanoparticles. The plasmonic and charging effects were differentiated by using Au@SiO_2 and Ag@TiO_2 NPs in DSSCs, which led to increased photocurrent and photovoltage, respectively.[1] In another exciting study, a significant photocurrent and efficiency enhancement in mesosuperstructured organometal halide perovskite solar cells incorporating core−shell Au@SiO_2 NPs delivering a device efficiency of up to 11.4% was shown. The authors attributed the enhanced photocurrents to the reduced exciton binding energy in the perovskite absorber from 100 to 35 meV upon incorporation of Au@SiO_2 core−shell NPs.[5] In yet another study, silica-coated nanocubes (Au@SiO_2) embedded in the photoanodes of DSSCs delivered a PCE of 7.8% relative to the 5.8% PCE of the reference (TiO_2 only) devices, resulting in a 34% improvement in the DSSC performance.[6] In another study, loading of silica-capped nanoprisms of Ag@SiO_2 in the titania photoanode resulted in a 32 ± 17% increase in the overall PCE of the device, driven primarily by an increase in the short-circuit current density. An 8.4% PCE was observed for their highest performing device, and this excellent performance was attributed to the Ag@SiO_2 nanoprisms.[7] In another investigation, asymmetric Au−SiO_2 clusters were integrated with the dye-sensitized ZnO nanosheets, and an efficiency of 2.24% was achieved compared to an efficiency of 1.79% for the control cell without the metal clusters.[8]

It is apparent from the consolidated overview of the recent developments in DSSCs with photoanodes incorporating metal nanostructures that, in order to make QDSCs competitive, it is imperative to develop novel photoanode architectures and counter electrodes, which can deliver PCEs comparable to those of other solar cell technologies. QDSCs offer several benefits over DSSCs, such as the possibility of producing more than one electron per impinging photon (also known as multiple-exciton generation), lower cost of QDs compared to dyes, and ease of tailoring the band gap by size control of the QDs, thus providing an opportunity to harvest the bulk of the visible and near-infrared (NIR) regions.[9−12] Despite these advantages, the achieved maximum PCE of QDSCs is less (about 5−6%)[13−16] due to insufficient loading of QDs over titania, their poor tethering with titana, and a high degree of back electron transfer. Incorporation of metal nanostructures in QDSCs is a facile and efficient approach for improving their PCEs. While Ag and Au nanostructures have been used exhaustively in DSSCs, the much cheaper, earth-abundant but equally effective Cu nanostructures have rarely been employed. Here, we present a low-cost but efficient design for a QDSC, wherein two different Cu nanostructures (NPs and nanoneedles (NNs)) prepared by a hydrothermal route were embedded in a TiO_2/CdS assembly, separately, and the effect of Cu NPs and Cu NNs on solar cell performances was studied. We used a highly conductive carbon fabric as a counter electrode, which is inexpensive compared to Pt, requires no elaborate treatment prior to use, unlike multiwalled carbon nanotubes (MWCNTs), and needs no iterative refluxing, washing, and centrifugation steps as in reduced graphene oxide, and therefore can be directly employed in a QDSC. QDSCs with photoanodes of TiO_2/CdS/Cu NPs and TiO_2/CdS/Cu NNs were assembled, and the conspicuous effects of Cu NNs and Cu NPs were discerned by unraveling the energetics of the systems by Kelvin probe force microscopy (KPFM) for the first time. The influence of Cu NPs and Cu NNs on light absorption via scattering effects, fluorescence, and excited electron lifetimes of CdS QDs was analyzed. The large differential in solar cell parameters, wherein the QDSCs based on TiO_2/CdS/Cu NNs outperform the cells based on TiO_2/CdS/Cu NPs by a large margin, is shown to be controlled by the different light-harvesting abilities of the two different photoanodes.

EXPERIMENTAL SECTION

Chemicals. Copper nitrate trihydrate ($Cu(NO_3)_2{\cdot}3H_2O$), ethylenediamine (EDA), hydrazine hydrate (H_6N_2O), sodium hydroxide (NaOH), cadmium acetate ($Cd(CH_3COO)_2$), sodium sulfide (Na_2S), acetylacetone, and solvents tetrahydrofuran (THF), toluene, and methanol were obtained from Merck. Titanium tetrachloride ($TiCl_4$) and Triton X-100 were procured from Aldrich. TiO_2 powder (P25) was a free gift from Evonik. Deionized water with a resistivity of ∼18.2 MΩ cm was used as a solvent. Inorganic transparent electrodes of SnO_2:F-coated glass (FTO, sheet resistance 25 Ω/sq) were obtained from Pilkington and were cleaned in a soap solution, 30% HCl solution, double-distilled water, and acetone, in that sequence, prior to use. Carbon fabric was procured from Alibaba Pvt. Ltd. and washed in acetone before use.

Synthesis of Cu Nanostructures. A 7 M NaOH solution (20 mL) was added to a 50 mL Teflon vessel, followed by 0.1 M copper nitrate (1 mL), ethylenediamine (150 μL) as the capping agent, and hydrazine hydrate (25 μL) as the reducing agent, in accordance with a method reported by Chang et al.[17] The color of the solution was clear. A constant alkaline pH of 14 was maintained, and this formulation was heated in an autoclave at a fixed temperature of 150 °C for different time durations of 1, 2, and 3 h. The Cu product obtained at the end of each heating period was collected individually and stored in the dark at room temperature.

Photoanode Preparation. Over the cleaned FTO-coated conducting glass plates, a TiO_2 paste made of TiO_2 powder (0.3 g) dispersed uniformly in a clear solution of acetylacetone (1.5 mL), ultrapure water (8.5 mL), and Triton X-100 (20 mg) was applied by doctor blading. The as-fabricated TiO_2 plates were heated at 60 °C for 30 min, followed by annealing at 500 °C for another 30 min. One more layer of TiO_2 was applied using the same steps as described above, followed by heating and annealing as performed for the active layer. The TiO_2-coated FTO substrate was finally immersed in an aqueous $TiCl_4$ (40 mM) solution for 30 min at 70 °C, and the ensuing TiO_2 film was washed in distilled water and annealed at 500 °C for 30 min. Over the TiO_2 film, CdS QDs were deposited by a successive ionic layer adsorption and reaction (SILAR) process. Two individual glass beakers were used, one containing 0.1 M cadmium acetate and another with 0.1 M sodium sulfide, both salts dissolved in methanol as cadmium and sulfide precursors. The TiO_2 films were initially immersed in the cadmium precursor for 2 min, then rinsed in methanol to remove excess ions, and then dried at 60 °C in a hot air oven. The same films were immersed in the sulfide precursor solution for 2 min and then rinsed in the solvent, and this is referred to as one SILAR cycle. The plate was subjected to six more SILAR cycles, and the resulting film is labeled as a TiO_2/CdS film.

Cu products (10 mg, Cu NPs or Cu NNs (obtained after 1 and 3 h of hydrothermal treatment)) were added to THF (10 mL) and sonicated for 5 min. A two-electrode configuration, wherein the TiO_2/CdS film served as the working electrode, a Pt rod served as the counter electrode, and the solution of Cu NPs or Cu NNs served as the medium, was used for the electrophoretic deposition of Cu NPs and Cu NNs on the photoanode. By application of a dc voltage of 30 V with a Tarsons electrophoresis power supply for different time spans of 2, 3, and 5 min, the Cu NPs or NNs were driven by the electric field through the pores of the yellow-orange-colored TiO_2/CdS assembly,

DOI: 10.1021/acsami.5b01175
ACS Appl. Mater. Interfaces 2015, 7, 13303−13313

and brown-colored electrodes of TiO_2/CdS/Cu NPs and TiO_2/CdS/Cu NNs were obtained. These electrodes were washed in THF, dried in a hot air oven at 45 °C for five days, and used. QDSCs were assembled in sandwich configurations with TiO_2/CdS or TiO_2/CdS/Cu NPs or TiO_2/CdS/Cu NNs as the photoanode, a 0.1 M Na_2S solution in ultrapure water, methanol (mixed in a 3:7, v/v, ratio) as the electrolyte, and a carbon fabric affixed on a microslide glass plate (with glue) as the counter electrode. An adhesive spacer of 2 mm thickness was applied along the four sides of the active area of the photoanode with an open port along one edge, and an open cavity was created. This cavity was closed by affixing the counter electrode over this assembly. The electrolyte was injected into the device through the open port, and the port was sealed using an inert polymer. A schematic illustrating photoanode preparation and device construction is shown in Scheme 1.

Scheme 1. Cartoon Showing the Preparation of a Photoanode Followed by QDSC Fabrication

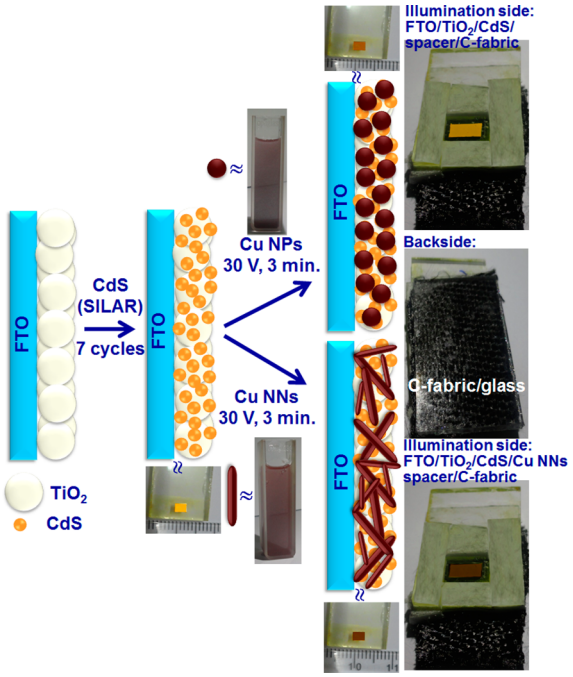

Characterization Techniques. Surface morphology analysis was performed using field emission scanning electron microscopy (FE-SEM; Carl Zeiss Supra 40). The optical absorption spectra of the TiO_2 and CdS films and TiO_2/CdS based films with/without Cu NPs or Cu NNs were measured in the diffuse reflectance mode and converted to absorbance using the Kubelka–Munk function, and for films of Cu NPs and Cu NNs, spectra were measured in the absorbance mode, all on a UV–vis–NIR spectrophotometer (Shimadzu UV-3600). Photoluminescence (PL) spectra of the films were measured on a Horiba Fluoromax-4 fluorescence spectrometer; a suitable filter was utilized during the measurement, and background correction was also applied. The time-correlated single-photon counting (TCSPC) method was used for deducing emission lifetimes with a Horiba Jobin Yvon data station hub functioning in the TCSPC mode. A nano light-emitting diode (nano-LED) emitting pulses at 370 nm with a 1 MHz repetition rate and a pulse duration of 1.3 ns was employed as the excitation source. Light-scattering Ludox solution (colloidal silica) was used to acquire the instrument response function (prompt). A long-pass 500 nm filter was placed in front of the emission detector for all measurements. Horiba Jobin Yvon DAS6 fluorescence decay analysis software was used to fit the model function (biexponential decays) to the experimental data, with appropriate correction for the instrument response. Transmission electron microscopy (TEM; model Tecnai G2, FEI, operating an accelerating voltage of 200 kV) was carried out by dispersing the samples in toluene and then transferring them onto carbon-coated copper grids. CdS electrodes were prepared by seven direct cycles of SILAR on FTO substrates. The film was scraped from the substrate, sonicated in toluene, then transferred to a carbon-coated copper grid, followed by solvent evaporation, and then used for the TEM study. Current versus potential (I–V) data of the QDSCs were measured using a Newport Oriel 3A solar simulator with a Keithley model 2420 digital source meter. The active areas of the photoanodes were in the range of 0.12–0.15 cm^2. For TiO_2/CdS, the average values for the solar cell parameters presented were based on data acquired from 10 cells. Data obtained from seven cells based on the TiO_2/CdS/Cu NN electrode and from six cells based on the TiO_2/CdS/Cu NP electrode were used for the average values presented. A 450 W xenon arc lamp was the light source, which provided a light intensity of 100 mW cm^{-2} of air mass (AM) 1.5G illumination; the spatial uniformity of irradiance was confirmed by calibration with a 2 cm × 2 cm Si reference cell and reaffirmed with a Newport power meter. Before collection of I–V data, each electrode was allowed to reach equilibrium at open circuit. IQEs and EQEs (internal and external quantum efficiencies) were recorded using a QE measurement system, Oriel IQE-200, capable of measurements compliant with ASTM (American Society for Testing and Materials) Standard E1021-06. The instrument gave the EQE and IQE directly as a function of the wavelength. The light source was a 250 W quartz tungsten halogen lamp. The monochromator path length was 1/8 m, and the rectangular spot size was 1 mm × 2.5 mm at the focus. Linear sweep voltammograms of Cu NNs and Cu NPs were recorded on an Autolab PGSTAT 302N equipped with NOVA1.9 software. A square cavity was constructed using an insulating adhesive foam tape on a stainless steel (SS) sheet. The cavity was filled with the sample, and another SS sheet was carefully placed over this assembly to complete the cell. This cell was used for linear sweep voltammetry (LSV); electrical contacts were taken from the SS electrodes, which were prevented from short-circuiting by the thick tape. A Veeco Multimode 8 microscope in ScanAsyst mode (Nanoscope 8.10 software) was used for AFM (atomic force microscopy) and KPFM measurements. In KPFM, a line scan was produced first in tapping mode, and then the same line was rescanned in the lift mode at a tip height of ∼150 nm. Antimony-doped silicon cantilevers with tips coated with Co/Cr were used. The probe tip had a radius of 10 nm, a spring constant of 0.2 N cm^{-2}, and a current sensitivity of 1 nA V^{-1}, and a load force of 50 nN was maintained between the tip and the sample. The sample was affixed onto a stainless steel disk with a conducting carbon tape. A thin strip of pinhole-free silver paste was used for making contacts. A bias voltage of $V_{tip} = V_{dc} + V_{ac} \sin \omega t$ (ω is the resonance frequency of the cantilever and V_{dc} and V_{ac} are the continuous and alternating voltages) was applied to the tip, while the sample was maintained at 1 V ground potential. A feedback loop incessantly attuned V_{dc} to cancel out the force between the tip and the specimen at frequency ω. V_{dc} was measured with varying positions, thus generating the surface potential map. Brunauer–Emmett–Teller (BET) specific surface area measurements were performed on a Micromeritics ASAP 2020 for Cu NPs and Cu NNs.

RESULTS AND DISCUSSION

Structural Studies. The FE-SEM images of Cu nanostructures, obtained by hydrothermal treatment from a solution of $Cu(NO_3)_2$ and additives in water, at the end of 1, 2, and 3 h are shown in Figure 1. The morphology is made of interconnected nanoparticles at the end of 1 h. This product was labeled as Cu nanoparticles (NPs). At the end of 2 h, a mixed morphology of Cu products is obtained. At this juncture, mingling Cu structures of elongated needle-like shapes and nanoparticles are observed. The low-magnification image of the Cu product produced after heating to 3 h shows the presence of NN-like shapes with hardly any particles in sight, and the corresponding high-magnification image shows the nanoneedles to have lengths in the range of 500–1200 nm. The morphology of

DOI: 10.1021/acsami.5b01175
ACS Appl. Mater. Interfaces 2015, 7, 13303–13313

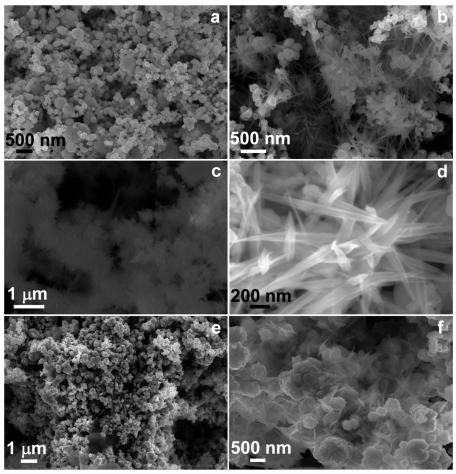

Figure 1. FE-SEM images of Cu products obtained after a precursor solution containing $Cu(NO_3)_2$, ethylenediamine, and hydrazine hydrate was heated in an autoclave at 150 °C for (a) 1 h, (b) 2 h, and (c, d) 3 h. Micrographs of (e) TiO_2/CdS/Cu NP and (f) TiO_2/CdS/Cu NN electrodes.

the TiO_2/CdS/Cu NPs shows interlinked, aggregated nanoparticles. Since all three components of this electrode, i.e., TiO_2, CdS QDs, and Cu NPs, exist in the form of nanoparticles, the particulate morphology is a natural consequence. The TiO_2/CdS/Cu NN electrode shows a granular structure which is interspersed with the needle-like shapes, indicative of the mixing of the Cu NNs with the TiO_2/CdS assembly. The XRD patterns of Cu NPs and Cu NNs obtained after 1 and 3 h of hydrothermal treatment of the Cu salt based precursor medium are shown in Figure S1 (Supporting Information). Both the patterns are almost similar; a broad hump is observed in the low 2θ region, indicating that the Cu NPs and NNs are not fully crystalline, and they are to some extent amorphous or nanocrystalline. For both samples, an intense peak observed at a d value of 2.09 Å corresponds to the (111) plane of the face-centered cubic (fcc) lattice of Cu, in concurrence with the powder diffraction file (PDF) number 031005. The remaining low-intensity broad peaks at d = 1.8, 1.2, and 1.09 Å were indexed to the (200), (220), and (311) planes of the fcc crystal structure of Cu. The TEM micrographs and the selected area electron diffraction (SAED) patterns of the Cu NPs and NNs and the films of TiO_2/CdS/Cu NPs and TiO_2/CdS/Cu NNs are displayed in Figure 2. The nanoneedles are clearly visible in the micrographs of Cu NNs; they are broad in the middle with pointed ends (Figure 2 a,b). The width of the nanoneedles varies from 10 to 25 nm, and their lengths are about 800−1300 nm. The morphology of the Cu NPs shows the presence of interlinked particles (Figure 2c). The SAED pattern of Cu NNs shows bright spots (Figure 2d), and these could be indexed to the (220) plane of the fcc lattice of Cu. The SAED pattern of Cu NPs (Figure 2e) shows diffuse rings, indicating that a higher degree of amorphicity prevails in the NPs compared to the NNs. The spots superimposed over the rings were indexed to the (111) and (200) reflections (Figure 2e). The micrograph of the TiO_2/CdS/Cu NNs (Figure 2f) shows the Cu nanoneedles tethered to the particulate morphology of TiO_2/CdS, and the TiO_2/CdS/Cu NP electrode (Figure 2g) is composed of aggregated particles. A lattice scale image of pristine CdS (extracted from a CdS film deposited by SILAR on FTO, Figure 2h) shows the CdS nanoparticles to be 2.5−5 nm in dimension, and the lattice

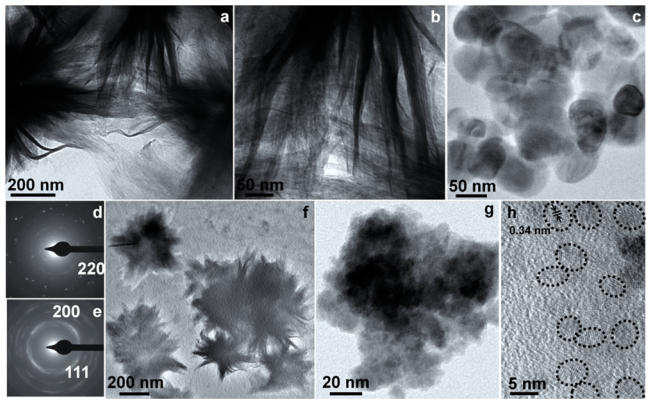

Figure 2. TEM images of (a, b) Cu NNs and (c) Cu NPs, SAED patterns of (d) Cu NNs and (e) Cu NPs, TEM images of (f) TiO_2/CdS/Cu NNs and (g) TiO_2/CdS/Cu NPs, and (h) lattice scale image of CdS QDs.

fringe separation is about 0.34 nm, which matches with an interplanar spacing of 3.36 Å, as per PDF number 652887 of CdS with an fcc crystal structure.

If electromagnetic radiation upon interaction with a quantum dot/metal nanoparticle assembly results in surface plasmon resonance (SPR) in a metal nanoparticle which is in the vicinity of the semiconducting QDs, then the collective surface electron oscillations typically undergo the following: The plasmon is reradiated (scattered as photons), and this localized optical energy is picked up by the QD in proximity, resulting in an enhanced absorption.[18] In addition, metal nanostructures of nanometric dimensions can scatter light, and this light is redirected into the photoactive material, which results in an increase in the optical path length of light. This translates to an increased absorption of the photoactive semiconductor. It has been established in the past, by theoretical and experimental studies, that, for gold particles, the scattering cross-section dominates the absorption cross-section at sphere dimensions of about 100 nm.[19] At particle sizes above 100 nm, the far-field scattering effect dominates; as a consequence, the scattered light is trapped within the material, and absorption of the quantum dot increases due to the increased optical path length. Since this particular dimension prerequisite is easily satisfied by the Cu NNs' (length wise) dimensions (0.8−1.3 μm), it is apparent that this far-field scattering enhancement can be tapped only in the photoanode containing Cu NNs (such as the TiO_2/CdS/Cu NNs). As a consequence, one can expect this photoanode to show increased absorption in comparison to TiO_2/CdS or TiO_2/CdS/Cu NPs in the NIR region. Cu NPs, on the other hand, vis-à-vis light scattering, due to their smaller size, can only increase the light absorption of semiconducting QDs (such as the TiO_2/CdS/Cu NP assembly) in the visible region, relative to that of the sole TiO_2/CdS electrode.

Absorption, Conduction, and Fluorescence Analysis. Cu nanoparticles and nanoneedles were electrophoretically deposited on transparent conducting electrodes, and their absorption spectra are shown in Figure 3a. The duration of deposition for Cu nanoparticles and nanoneedles was fixed at 3 min, on the basis of maximum absorption enhancement induced in the visible and NIR regions of a TiO_2/CdS assembly, upon their incorporation by electrophoresis. At durations shorter and longer than this period, the absorption increment of TiO_2/CdS was lesser. The films of both pristine Cu nanostructures show a strong broad absorption peak at

DOI: 10.1021/acsami.5b01175
ACS Appl. Mater. Interfaces 2015, 7, 13303−13313

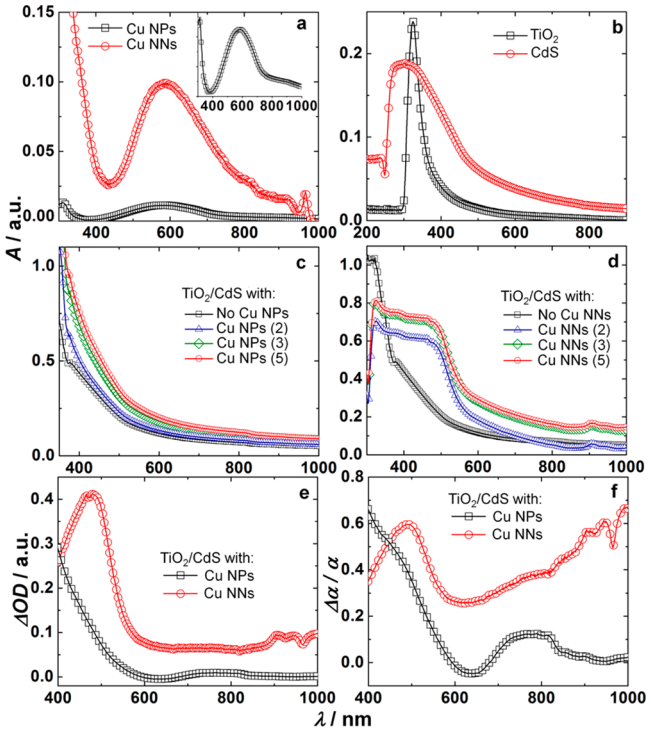

Figure 3. (a) Absorbance spectra of (a) Cu NPs (□) and Cu NNs (○) deposited in the form of thin films on glass substrates (the inset of (a) is a magnified view of the absorption of Cu NPs), (b) films of pristine TiO_2 (□) and pristine CdS (○), (c) films of TiO_2/CdS without Cu NPs embedded (□) and with Cu NPs embedded by electrophoresis for 2 (△), 3 (○), and 5 (◇) min, and (d) films of TiO_2/CdS without Cu NNs embedded (□) and with Cu NNs embedded by electrophoresis for 2 (△), 3 (○), and 5 (◇) min. (e) OD change and (f) $\Delta\alpha/\alpha$ (absorption coefficient change) induced by Cu NPs (□) and Cu NNs (○) in a TiO_2/CdS film by their incorporation through electrophoresis for 3 min.

~584 nm, and the nanoneedles show an additional peak at 964 nm. These arise from the transverse and longitudinal modes corresponding to the short and long axes of the nanostructures. In the film of Cu nanoparticles, due to the absence of the long axis, the absorption in the NIR region is not observed. The absorption spectra of pristine TiO_2 and CdS electrodes are shown in Figure 3b, and the optical band gaps deduced from their absorption band edges are 3.1 and 2.3 eV, respectively. The absorption spectra of the TiO_2/CdS, TiO_2/CdS/Cu NP, and TiO_2/CdS/Cu NN photoanodes are shown in Figure 3c,d. The TiO_2/CdS electrode shows its band edge absorption in the 400−500 nm wavelength region, and upon electrophoretic inclusion of Cu NPs and Cu NNs in these films for different durations of 2, 3, and 5 min, the highest absorption increment for the TiO_2/CdS electrode was achieved at a 3 min duration for both Cu nanostructures, indicating that this duration of electrophoresis results in an optimum concentration of Cu NPs and Cu NNs. The absorption of the TiO_2/CdS electrode increases significantly in the 400−550 nm wavelength range and also in the NIR region between 880 and 930 nm upon inclusion of CdS NNs in the film, indicating that the light scattering effect of the Cu NNs increases the optical absorption of the QD based electrode. The absorption increment induced by the Cu NNs at both visible and NIR wavelengths is blue-shifted compared to the absorption peaks of pristine Cu NNs at 584 and 964 nm. The blue shift could be due to the increased electron density in the Cu NNs, a consequence of photoexcited electron transfer from TiO_2/CdS to Cu NNs via Fermi level equilibration, which is discussed in detail later. This frequency is directly proportional to the electron density in the metal nanoparticles, and therefore, the blue shift is explained. A similar blue shift was previously observed by Choi et al. for Au@TiO_2 nanoparticles due to electron injection from TiO_2 to Au nanoparticles upon photoirradiation.[1] In the case of the TiO_2/CdS/Cu NP electrode, absorption is moderately increased compared to that of the pristine TiO_2/CdS electrode in the 400−500 nm wavelength regime, suggesting that Cu NNs as opposed to Cu NPs are more effective in improving the optical absorption of the QDs via light-scattering effects. To further quantify the effect of scattering by Cu nanostructures, the ΔOD (optical density change; $\Delta OD = OD_{TiO_2/CdS/Cu\ NN/NP} - OD_{TiO_2/CdS} - OD_{Cu\ NN/Cu\ NP}$) and $\Delta\alpha/\alpha$ (relative absorption coefficient change; $\Delta\alpha/\alpha = OD_{TiO_2/CdS/Cu\ NN/NP} - OD_{TiO_2/CdS} - OD_{Cu\ NN/Cu\ NP}/OD_{Cu\ NN/Cu\ NP}$) effected in TiO_2/CdS by Cu NNs and Cu NPs were plotted as a function of the wavelength and are shown in Figure 3e,f. A similar method for determining the enhancement in a Ru dye's absorption in TiO_2/dye/Ag@TiO_2 NPs was used by Qi et al.[3] The ΔOD and $\Delta\alpha/\alpha$ magnitudes were larger for the Cu NN based electrodes relative to the Cu NP based electrodes. The net absorption of CdS QDs is greatly increased by Cu NNs compared to Cu NPs, at both photopic and NIR wavelengths.

The linear sweep voltammograms of Cu NPs and Cu NNs are shown in Figure 4. The Cu NNs and Cu NPs were filled in

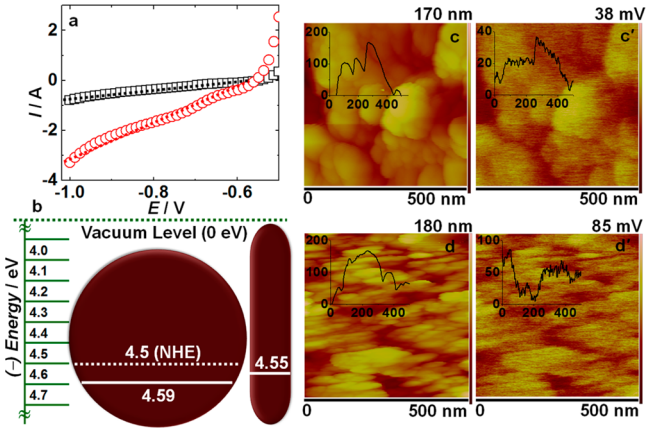

Figure 4. (a) LSV plots of Cu NPs (□) and Cu NNs (○). The dotted lines represent the linear fits. (b) Schematic showing the Fermi levels of Cu NPs and Cu NNs deduced from KPFM. (c) Simultaneous topography and surface potential maps of films of (c, c′) Cu NPs and (d, d′) Cu NNs obtained from KPFM. The insets of the images are the corresponding representative section profiles.

a rectangular cavity created by an adhesive (tape) spacer of 0.2 cm^2 dimension and 0.25 cm thickness. The variation of current produced as a function of the applied bias is quasi-linear in the −1.0 to −0.6 V potential domain for both the samples. From the corresponding linear fits, by assuming Ohmic dependence, the bulk conductivities of the two samples were determined by using the equation $\kappa = (I/V)(l/a)$, where l is the thickness of the sample (spacer thickness), a is the area of the active material (geometric area of the cavity), and I/V is the slope obtained from the linear fit. The ambient temperature electrical conductivities of Cu NPs and Cu NNs were calculated to be 2

DOI: 10.1021/acsami.5b01175
ACS Appl. Mater. Interfaces 2015, 7, 13303−13313

and 9 S cm^{-1}, respectively. The conductivity of Cu NNs is 4.5 times greater than that of the Cu NPs; the elongated structures of Cu NNs allow facile unhindered charge propagation, whereas the charge movement is constrained in Cu NPs due to the presence of a larger number of grain boundaries, and therefore, the electrical conductivity is lower for the latter. A larger electrical conductivity implies that photogenerated electron movement will be relatively unobstructed for Cu NNs compared to Cu NPs when they are integrated with the TiO_2/CdS assembly.

The fluorescence spectra of CdS/glass and electrodes of TiO_2/CdS, TiO_2/CdS/Cu NPs, and TiO_2/CdS/Cu NNs deposited on FTO/glass obtained at an excitation wavelength of 370 nm are shown in Figure 5a. The photoluminescence of

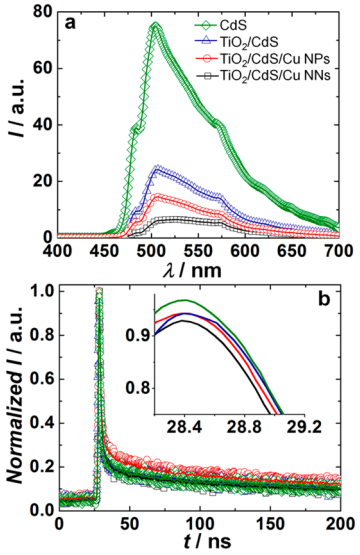

Figure 5. (a) Fluorescence spectra of films of CdS/glass (◇) and TiO_2/CdS/FTO (△), TiO_2/CdS/Cu NPs/FTO (○), and TiO_2/CdS/Cu NNs/FTO (□) glass, wherein Cu NPs were incorporated into TiO_2/CdS through electrophoresis for 3 min. (b) Time-resolved fluorescence decay traces of CdS/glass (◇) and TiO_2/CdS/FTO (△), TiO_2/CdS/Cu NPs/FTO (○), and TiO_2/CdS/Cu NNs/FTO (□) films. The inset of (b) represents the corresponding enlarged views of the decay profiles. The excitation wavelength was fixed at λ_{ex} = 370 nm in (a) and (b), and λ_{em} was fixed at 500 nm in (b).

CdS QDs is broad and spans from 450 to 650 nm, with a λ_{max} at ~505 nm, which corresponds to the band edge emission, in accordance with literature reports on CdS films deposited by SILAR.[20] The PL spectrum was deconvoluted into five components at 480, 500, 529, 572, and 622 nm. The multiple components are attributed to the defects present in the dots. The PL response of CdS is quenched when the QDs are anchored to titania in the TiO_2/CdS electrode as the photogenerated electrons in CdS cascade from the conduction band (CB) of CdS (poised at 3.9 eV) into the conduction band of TiO_2 (located at 4.2 eV). The CdS fluorescence profile retains about 32% of its original intensity in the presence of titania. Upon further introduction of Cu NNs or Cu NPs into the TiO_2/CdS assembly, the fluorescence of CdS is quenched to 19% and 10%, respectively, of the original value of pristine CdS, and since the emission of the TiO_2/CdS/Cu NN system was the lowest among those of the four electrodes, it is obvious that Cu NNs are more adroit in accepting photoelectrons from CdS compared to Cu NPs. The mechanism of excited electron deactivation in CdS was further confirmed by time-resolved emission decay experiments. The emission decay traces were acquired for CdS/glass and electrodes of TiO_2/CdS, TiO_2/CdS/Cu NNs, and TiO_2/CdS/Cu NPs at an excitation wavelength of 370 nm, with the emission fixed at 500 nm, close to the steady-state emission maximum, and these plots are shown in Figure 5b. The decay curves accurately fit into biexponential functions, and the average electron lifetimes ($\langle\tau\rangle$) were determined and are listed in Table 1.

$$I = B_1 \exp(-t/\tau_1) + B_2 \exp(-t/\tau_2) \quad (1)$$

$$\langle\tau\rangle = \sum B_i\tau_i^2 / \sum B_i\tau_i \quad (2)$$

In eqs 1 and 2, B_1 and B_2 are the amplitude coefficients of the excited electron lifetimes (τ_1 and τ_2) and t is the time after LED excitation. For CdS QDs, the short- and the long-lived components of 0.4 and 14.4 ns correspond to electron−hole recombination at the band edge and trap states. Trap states are typically located at the interparticle interfaces, and they constitute the midgap states. Recombination by trapping of an electron in the midgap states is slower than recombination with the hole created in the valence band after excitation, hence the corresponding assignments. The short-lived component in each of the three electrodes TiO_2/CdS, TiO_2/CdS/Cu NPs, and TiO_2/CdS/Cu NNs is due to the photogenerated electron depopulation pathway via electron transfer from the CB of CdS to the equilibrated Fermi level of the TiO_2/CdS/Cu NN or NP based electrode or to the CB of TiO_2 in the TiO_2/CdS electrode. In the electrodes encompassing Cu NNs and Cu NPs, there are two possible causes of decay corresponding to the short-lived component: it is attributed to the excited electron transfer from the CB of CdS to the (i) equilibrated Fermi level of the photoanode and (ii) to the CB of TiO_2. Since the data fit best in a biexponential function, these two modes cannot be resolved further. The short-lived time constant is greater than 1 ns for both TiO_2/CdS/Cu NPs and TiO_2/CdS/Cu NNs, and therefore, it cannot be assigned to charge transfer by cascade. The slow decay component in each of the above electrodes therefore arises from the band edge electron−hole recombination in CdS QDs. The average electron lifetime is the lowest for the TiO_2/CdS/Cu NNs electrode, which confirms that excited electron deactivation is the fastest in this electrode.

Study of Energetics. The equilibrated Fermi level in the electrodes of TiO_2/CdS/Cu NNs and TiO_2/CdS/Cu NPs was determined by KPFM measurements. When a charged semiconductor such as TiO_2 or CdS is brought into contact

Table 1. Kinetic Parameters of Emission Decay Analysis of Photosensitizer Films Deduced from Double-Exponential Fits

sample	B_1	τ_1 (ns)	B_2	τ_2 (ns)	$\langle\tau\rangle$ (ns)	χ^2
CdS	61.46	0.381	38.54	14.4	13.83	0.932
TiO_2/CdS	37.4	9.92	62.6	0.365	9.363	1.03
TiO_2/CdS/Cu NPs	13.84	1.54	86.16	0.231	0.91	1.13
TiO_2/CdS/Cu NNs	99.99	0.0052	0.01	4.89	0.422	1.03

DOI: 10.1021/acsami.5b01175
ACS Appl. Mater. Interfaces 2015, 7, 13303−13313

with a metal nanostructure, the Fermi levels of the two equilibrate, and the Fermi level shifts close to the CB of the semiconductor. A Fermi level shift by −22 mV (toward more negative potentials versus the normal hydrogen electrode, NHE) was earlier observed for a TiO_2/Au NP system, wherein electrons are transferred from the CB of UV-irradiated TiO_2 to Au NPs via the equilibrated Fermi level.[21] Successive AFM (topography) and KPFM (surface potential (SP)) images acquired for the solid-state films of Cu NPs, Cu NNs, TiO_2/CdS/Cu NNs, and TiO_2/CdS/Cu NPs are shown in Figures 4 and 6. The images were obtained using a Co/Cr tip of a known

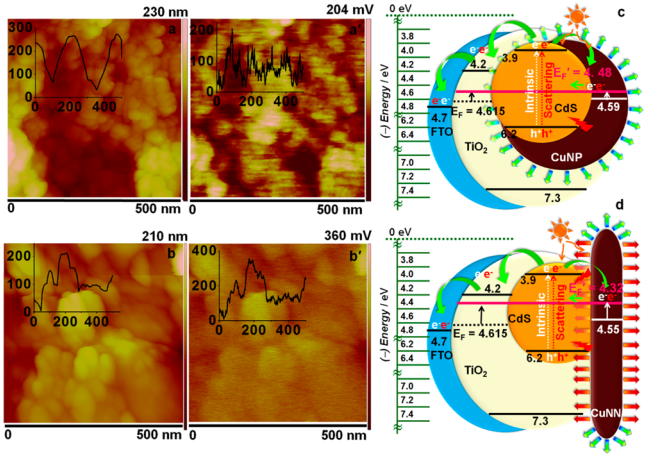

Figure 6. Concurrent topography and surface potential maps of (a, a′) TiO_2/CdS/Cu NP and (b, b′) TiO_2/CdS/Cu NN electrodes obtained by KPFM. The insets of the images are the corresponding representative section profiles. Energy band diagrams illustrating the Fermi level upshift to more negative potentials versus NHE induced by (c) Cu NPs in the TiO_2/CdS/Cu NP electrode and (d) Cu NNs in the TiO_2/CdS/Cu NN electrode.

work function. KPFM furnishes a localized measure of the contact surface potential difference between the conductive tip and the electrode surface. SP is defined as $SP = \phi_{tip} - \phi_{sample}/q$, where ϕ_{tip} and ϕ_{sample} are the work functions of the tip and sample, respectively, and q is the electronic charge. The tip was calibrated using a standard sample of highly ordered pyrolytic graphite (HOPG), having a known work function of 4.6 eV, and as a result, the SP equation takes the following form:

$$\varphi_{sample} = 4.6 + SP_{HOPG} - SP_{sample} \quad (3)$$

The work functions of the films of Cu NPs and Cu NNs were determined to be 4.59 and 4.55 eV, and they are illustrated in Figure 4b. The work function of Cu NNs is shallower than that of Cu NPs, and the impact of this difference is such that, upon integration with the TiO_2/CdS electrode, the Cu NNs raise the equilibrated Fermi level to more negative potentials versus NHE compared to Cu NPs. This is also reflected clearly in the experimental values obtained for the TiO_2/CdS/Cu NP and TiO_2/CdS/Cu NN electrodes; they were 4.48 and 4.32 eV (Figure 6a′,b′). These can be regarded as the apparent or equilibrated Fermi levels (E_F') for the films and were used for expounding the charge transfer mechanisms in the two photoanodes, as shown in the energy band diagram shown in Figure 6c,d. Cu NPs and Cu NNs are deposited after the deposition of CdS over TiO_2; therefore, the Fermi level equilibration will occur dominantly between Cu NPs or Cu NNs and CdS QDs. At the same time, one more factor should be considered. The coverage of CdS over TiO_2 is not absolute (one of the foremost reasons for the lower efficiencies of QDSCs compared to DSSCs); therefore, there are sites available on TiO_2 to which Cu NPs or Cu NNs can tether. This is also supported by the presence of large pores (30−300 nm in dimension, with an average size of about 120 nm) in the CdS/TiO_2 film (Figure S2, Supporting Information), which allows the easy percolation of Cu NPs, which are 50−90 nm in dimension. Cu NNs are on average 30 nm in width and 800−1300 nm long, so permeation through the TiO_2 matrix is feasible in a vertical manner.

When CdS QDs come into contact with Cu NNs or CuNPs, the Fermi level shifts to more negative potentials (versus NHE), toward the conduction band of CdS. The Fermi level position of pristine Cu NPs is 4.59 eV, and that of pristine Cu NNs is 4.55 eV. After the incorporation of Cu NPs or Cu NNs in the TiO_2/CdS film, the equilibrated Fermi levels of the resulting TiO_2/CdS/Cu NP and TiO_2/CdS/Cu NN films shift upward. Excited electrons (intrinsic and Cu NPs/Cu NNs, scattering induced) from CdS, upon illumination, are transferred to TiO_2. This is supported by earlier studies on TiO_2/Au systems.[22,23] The authors[22,23] stated that, in the case of semiconductor nanocrystals, such as an electrode made up of TiO_2 nanocrystals (sensitized by Au nanoparticles), the electrons are confined and the individual nanocrystal remains isoenergetic. Due to this size limitation, the bands remain flat and the charge separation is essentially dictated by the Fermi level equilibration.[22,23] Therefore, band bending does not occur in semiconductor nanostructures (as in TiO_2/CdS in our case) in contact with metal nanostructures (such as Cu NNs and NPs in the present case). Furthermore, due to Fermi level equilibration, particularly between CdS and Cu NPs or NNs, the extent of e^-−h^+ recombination within CdS is also expected to decrease. For now, excited electrons in CdS have an additional deactivation pathway via Cu NPs or NNs which is unavailable in the sole TiO_2/CdS assembly.

The Fermi level of pristine TiO_2 was also determined by KPFM. The simultaneous topography and surface potential maps of a TiO_2 film are shown in Figure S3 (in the Supporting Information). The average value for the surface potential was 6 mV, and using eq 3, the work function or the Fermi level of pristine TiO_2 was calculated to be 4.615 eV. When in contact with CdS/Cu NPs or CdS/Cu NNs and/or Cu NPs or Cu NNs directly, the Fermi level of TiO_2 shifts upward toward more negative potentials as shown in the energy band diagram below. One piece of indirect evidence which supports this claim is the higher V_{OC} of the cells based on the electrodes containing Cu NPs or Cu NNs compared to that of the cell based on the sole TiO_2/CdS electrode. V_{OC} is the measure of the difference between the Fermi level of TiO_2 and the redox potential of the electrolyte. Since the electrolyte we used was the same for all three films, it is the photoanode's Fermi level governed by its composition which controls the V_{OC}.

Furthermore, the electrical conductivity of Cu NNs is better than that of Cu NPs, which also contributes to rapid electron injection into FTO. Compared to the Cu NPs, Cu NNs have a higher surface area and a higher electronic conductivity. As the effective surface area increases for the same geometric area, the interparticle contact between the Cu NNs and their connectivity with TiO_2 and CdS will increase, which will allow unhindered charge transport to the current collector. The surface areas of Cu NPs and Cu NNs were determined by BET studies (by nitrogen adsorption) and found to be 7.8 and 16.6

DOI: 10.1021/acsami.5b01175
ACS Appl. Mater. Interfaces 2015, 7, 13303−13313

$m^2\ g^{-1}$. The energy level gradient between FTO (ϕ_{FTO} = +0.2 V versus NHE or 4.7 eV) and the E_F' of TiO_2/CdS/Cu NPs is 0.22 eV, and that between FTO and the E_F' of TiO_2/CdS/Cu NNs is 0.38 eV. The energy level gradient is a direct measure of the driving force available to the system for electron injection from the E_F' to FTO. This energy gradient in terms of electromotive force can be expressed as +0.02 and +0.18 V versus NHE, respectively, for the TiO_2/CdS/Cu NP and TiO_2/CdS/Cu NN electrodes. It is well-known that $\Delta G^\circ = -nFE^\circ$, where ΔG° is the standard Gibbs free energy change for a reaction involving n electrons, F is Faraday's constant, and E° is the standard electrochemical potential. A thermodynamically favorable spontaneous process typically involves a large negative value for ΔG°. In compliance with the Marcus model, E° for the present system is the energy level gradient,[24] and since the energy gradient is larger for the TiO_2/CdS/Cu NN electrode, the magnitude of the associated ΔG° will be more negative. As a consequence, electron injection is faster for this system in comparison to the TiO_2/CdS/Cu NP electrode. The electron transfer process is therefore more spontaneous for the TiO_2/CdS/Cu NNs electrode, and therefore, the photoelectrochemical performance of the solar cell based on the TiO_2/CdS/Cu NN electrode is expected to be superior.

We had earlier observed that not only is the optical absorption of the TiO_2/CdS assembly enhanced when Cu nanostructures are enmeshed therein, but the overall absorption enhancement is blue-shifted compared to the SPR peak of Cu NPs or NNs. The increase in electron density in the Cu core due to electron injection from CdS to the equilibrated Fermi levels in the TiO_2/CdS/Cu nanostructure electrodes is responsible for the blue shift, which was observed earlier. The lowered electron lifetimes in the TiO_2/CdS/Cu NNs and TiO_2/CdS/Cu NPs compared to TiO_2/CdS are also indicators of electron transfer from the CB of CdS to the apparent Fermi levels of the photoanodes, induced by Cu NNs or Cu NPs. The first-order rate kinetics of electron transfer were determined for the two systems using the following relations:

$$k_{et} = 1/\langle\tau\rangle(TiO_2/CdS/CuNPs) - 1/\langle\tau\rangle(TiO_2/CdS) \quad (4)$$

$$k_{et} = 1/\langle\tau\rangle(TiO_2/CdS/CuNNs) - 1/\langle\tau\rangle(TiO_2/CdS) \quad (5)$$

The electron transfer rate constants were deduced to be 1.00 and 2.39 s^{-1} for the TiO_2/CdS/Cu NP and TiO_2/CdS/Cu NN electrodes. The rate constant is 2.39 times greater for the system with Cu NNs. The electron injection rate is faster in the assembly with Cu NNs, which reiterates the ability of Cu NNs to favorably impact the photocurrent collection of the TiO_2/CdS electrode.

Photoelectrochemical Studies. The light-scattering effect of Cu NPs and Cu NNs was confirmed by assembling quantum dot solar cells with TiO_2/CdS, TiO_2/CdS/Cu NP and TiO_2/CdS/Cu NN electrodes as the photoanodes, a solution of 0.1 M Na_2S in ultrapure water/methanol (3:7, v/v) as the electrolyte, and a carbon fabric as the counter electrode. The thicknesses of the three TiO_2/CdS, TiO_2/CdS/Cu NP, and TiO_2/CdS/Cu NN electrodes were 9.1, 9.44, and 9.4 μm, respectively. These thicknesses were determined by cross-sectional SEM studies (Figure S4, Supporting Information). The carbon fabric has a sheet resistance of 10 $\Omega\ cm^{-2}$, and offers a conductance of 0.625 S (Figure S5, Supporting Information). These values are acceptable for bringing about the reduction of the oxidized electrolyte species upon illumination. The morphology of the fabric is comprised of a crisscross, meshlike structure of carbon fibers, which is easily wetted by the electrolyte. The work function of carbon is about 4.5 eV, which is similar to that of reduced graphene oxide (RGO) and MWCNTs, which have been used exhaustively as counter electrodes in QDSCs.[25,26] Compared to MWCNTs and RGO, it is much easier to handle the carbon fabric, because no treatment with acids is required, as in MWCNTs, and no procedures such as the time-consuming multistep exfoliation of graphite is needed (as in RGO). The fabric is also cheap, and can be used directly in a QDSC without any preceding treatment by simply snipping it out in the desired dimensions, advantages which are very attractive for fabrication of low-cost solar cells. The reason for using a methanol based electrolyte over an aqueous one was the superior and stable solar cell performance achieved in such an electrolyte compared to an aqueous one. The $J-V$ characteristics for a TiO_2/CdS photoanode in an aqueous solution of Na_2S were compared with those in a 3:7 (v/v) water/methanol electrolyte. The $J-V$ plots and the associated parameters are shown in Figure S6 and Table S1 (Supporting Information). For the cell examined in the aqueous medium, after 3 h of discontinuous exposure to 1 sun of irradiance, the PCE decreases from 2.387% to 2.146%, which is equal to a 10% drop. For the cell examined in the methanol/water solution, the PCE decreased from 2.67% to 2.41%, which amounts to a 9.74% decline in efficiency. More than the nature of the electrolyte medium, it is the decomposition of the dots in an alkali, induced by the irradiance, which causes the PCE to drop. This justified the use of a methanol based electrolyte for our studies. At the same time, the ability of methanol to scavenge holes also needs to be considered.[27] In an earlier study on the role of methanol in a photocatalytic hydrogen generation system, methanol was shown to be a "sacrificial hole scavenger". In an alkaline medium, it can, in principle, accept holes from the photoanode and undergo a series of reactions, which result in the formation of formaldehyde and hydrogen evolution.[27] Therefore, methanol as a sacrificial hole scavenger in our cells can have an adverse impact on the PCEs in the long run. More detailed studies will be undertaken in the future, such as the use of a protective ZnS layer to address this issue.

The $J-V$ characteristics of QDSCs with different photoanodes are shown in Figure 7a, and the solar cell parameters are summarized in Tables 2 and S2 (Supporting Information). The V_{OC} (open-circuit voltage) values of the three best performing cells are comparable, and vary from ~876 to 919 V, and the J_{SC} (short-circuit current density) values are in the range of ~8−10 mA cm^{-2}. The best performing QDSC is based on TiO_2/CdS/Cu NNs and shows a V_{OC} = 919.5 V, an FF (fill factor) = 0.47, a J_{SC} = 10.02 mA cm^{-2}, and an overall PCE (or η) of 4.36%. The average value of the net PCE is also larger for the TiO_2/CdS/Cu NN based cell compared to QDSCs based on TiO_2/CdS and TiO_2/CdS/Cu NPs. The best PCEs for the Cu NN and Cu NP based cells are greater by 56.8% and 18.7% compared to that of the TiO_2/CdS based cell. The highest PCE of the Cu NN based cell is larger by 32% compared to that obtained for the Cu NP based cell. It is apparent that while both Cu NPs and Cu NNs increase the PCE of the TiO_2/CdS based cell, Cu NNs are more effective in improving the PCE.

Here, we observed an increase in both V_{OC} and J_{SC} by ~43 mV and 1.24 times for the TiO_2/CdS/Cu NN based cell compared to the TiO_2/CdS based cell. Similarly, the V_{OC} and

DOI: 10.1021/acsami.5b01175
ACS Appl. Mater. Interfaces 2015, 7, 13303−13313

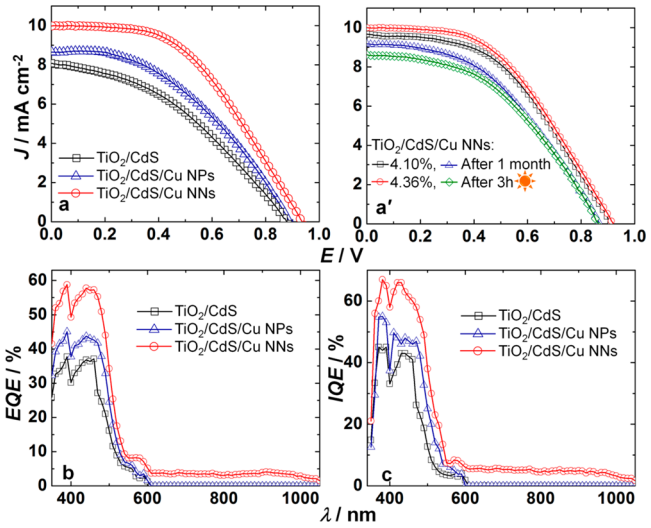

Figure 7. (a) $J-V$ characteristics (measured under 1 sun of illumination, AM 1.5G). (b) EQE and (c) IQE of QDSCs with the following photoanodes: TiO_2/CdS (□), TiO_2/CdS/Cu NPs (△), and TiO_2/CdS/Cu NNs (○). All experiments in (a)−(c) were performed for sandwich cells containing 0.1 M Na_2S in an ultrapure water/methanol (3:7, v/v) solution as the electrolyte and a carbon fabric assembly as the counter electrode. In (b) and (c), a 250 W tungsten−halogen lamp was used for illumination. (a′) $J-V$ characteristics of QDSCs with TiO_2/CdS/Cu NNs as the photoanode: as-fabricated with η = 4.36% (○), as-fabricated with η = 4.1% (□), η = 4.36% cell after 3 h of discontinuous illumination (◇), and η = 4.1% cell after 1 month of storage (△).

J_{SC} are enhanced by 14.4 mV and ∼1.1 times for the TiO_2/CdS/Cu NP based cell with respect to the TiO_2/CdS based cell. It is obvious that light scattering enabled by Cu NNs increases the net light absorption of the TiO_2/CdS assembly, and as a result, a greater number of photoexcited electrons are produced, which translates into a higher photocurrent. Since the far-field scattering component is only prevalent in the TiO_2/CdS/Cu NN based cell, the photocurrent is higher compared to tha tof the TiO_2/CdS/Cu NN based cell. The open-circuit voltage, in particular for the TiO_2/CdS/Cu NN electrode, is high, but there are reports on QDSC based CdS wherein the authors have achieved open-circuit voltages of 1.2 V,[28] 1.19 V,[29] and 1.27 V[30] in the past. Fast hole transfer to the electrolyte,[31] a shift of the Fermi level of TiO_2 to more negative potentials (versus NHE),[21] and a built-in chemical potential within the photoanode[32,28] upon illumination are touted as the reasons for the high V_{OC} values in the QDSCs.

Using photovoltage transient decay measurement experiments on QDSCs, it was shown that the magnitude of the open-circuit voltage is directly proportional to the time taken by the photoanode to undergo a photovoltage decay in the "light off" cycle after the photovoltage has stabilized in the "light on" cycle. The greater the time taken by the photovoltage to decay, the slower the recombination and the greater the charge density buildup ($\propto V_{OC}$) in the photoanode. We compared the photovoltage decay times for QDSCs based on the three electrodes under consideration, TiO_2/CdS, TiO_2/CdS/Cu NPs, and TiO_2/CdS/Cu NNs, by illumination under 0.5 sun, allowing the photovoltage to stabilize and then monitoring the photovoltage decay in the dark. The photovoltage decay plots are shown in Figure 8. The photovoltage at

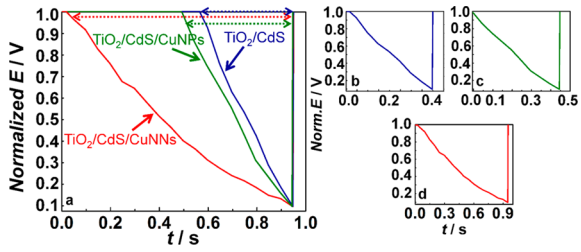

Figure 8. (a) Normalized photovoltage (from 1 V) versus time in the dark under the "light off" condition acquired after the photovoltage has stabilized for cells based on different photoanodes. (b)−(d) are the same plots shown independently from E = 1 V and t = 0 s for TiO_2/CdS, TiO_2/CdS/Cu NPs, and TiO_2/CdS/Cu NNs, respectively.

the start of the measurement was normalized to 1 V for all three cells on the ordinate axis, and the evolution of the voltage as a function of time for the three cells was studied. Transient photovoltage decays for a PbS/ZnO system by Ehrler et al.[33] and Shalom et al.[34] were plotted in previous studies; our trends match the reported trends, although the reported time scales are much lower. We observed that, for the photovoltage to drop by the same extent, the cell based on the TiO_2/CdS/Cu NN electrode takes 0.937 s, whereas cells based on the TiO_2/CdS and TiO_2/CdS/Cu NP electrodes take 0.389 and 0.456 s, respectively. This is one of the reasons for the higher open-circuit voltage registered for the cell based on the TiO_2/CdS/Cu NN electrode.

The higher V_{OC} values obtained for the cells containing Cu NNs and Cu NPs relative to the cell without either of them is also indirect proof of the role of Cu NNs and Cu NPs in serving as electron acceptors, because due to Fermi level equilibration induced by the these nanomoieties, the apparent Fermi level shifts to more negative potentials (versus NHE) relative to the Fermi level in the TiO_2/CdS electrode. The magnitude of the Fermi level to redox potential (of the electrolyte) difference (ΔE) obeys the following order: ΔE(TiO_2/CdS/Cu NNs) > ΔE(TiO_2/CdS/Cu NPs) > ΔE(TiO_2/CdS). The highest V_{OC} achieved in the TiO_2/CdS/Cu NN based cell is a manifestation of this Fermi level shift. The stability of the TiO_2/CdS/Cu NN based cell was determined by subjecting one cell with an efficiency of 4.36% to 3 h of discontinuous illumination and another cell with an efficiency of 4.1% to 1 month of storage under dark conditions (Figure 7a′ and Table S3 (Supporting Information)). The 4.36% efficient cell's efficiency dropped by 23.3% of its original

Table 2. Solar Cell Parameters of Cells with 0.1 M Na_2S Electrolyte with the Listed Photoanodes[a]

photoanode configuration	V_{OC} (mV)	J_{SC} (mA cm^{-2})	FF	η_{best} (%)	η_{av} (%)
TiO_2/CdS	876.6	8.07	0.39	2.78	2.715 ± 0.065
TiO_2/CdS/Cu NPs	891.0	8.66	0.43	3.30	3.15 ± 0.15
TiO_2/CdS/Cu NNs	919.5	10.02	0.47	4.36	4.23 ± 0.13

[a]Exposed cell area 0.12−0.15 cm^2, under 1 sun of illumination (100 mW cm^{-2}). All cells with a carbon fabric as the counter electrode.

DOI: 10.1021/acsami.5b01175
ACS Appl. Mater. Interfaces 2015, 7, 13303−13313

value to 3.345% upon illumination, and the 4.1% efficient cell's efficiency decreased by 14.4% and became 3.51%. It is apparent that photodecomposition has a stronger deleterious impact on the QDSC performance compared to prolonged storage. Detachment of the active material from the current collector is the primary reason for the performance decline, and this peeling off is triggered by extended illumination or exposure to aging. Methanol working as a hole scavenger can also contribute to the lowering of the cell performance.

The EQE and IQE versus wavelength plots of QDSCs based on TiO_2/CdS, TiO_2/CdS/Cu NP, and TiO_2/CdS/Cu NN electrodes are displayed in Figure 7b,c. EQE is defined as the ratio of the number of charge carriers collected by the cell to the number of photons of a given wavelength impinging upon the cell. While EQE is inclusive of optical losses such as transmission and reflection, IQE is defined as the efficiency with which photons that are not reflected or transmitted out of the cell can generate collectable carriers. The highest EQE in the visible region is exhibited by the cell based on TiO_2/CdS/Cu NNs (58% at 435 nm), followed by cells based on TiO_2/CdS/Cu NPs (44.5%) and TiO_2/CdS (38%). EQE is appreciably high (>25%) in the 350−520 nm wavelength range for the cell based on TiO_2/CdS/Cu NNs. In the same wavelength domain, it lies in the range of 15−37% and between 20% and 45% for the cells based on TiO_2/CdS and TiO_2/CdS/Cu NPs. The enhancement in EQE in the 350−500 nm wavelength regime observed for the TiO_2/CdS/Cu NN based cell compared to TiO_2/CdS and TiO_2/CdS/Cu NP based cells is a ramification of the light scattering induced by the Cu NNs and the Cu NPs. Light is ushered back by these nanostructures into the photoanode, wherein it is recaptured by the CdS QDs, and the population of the excited electrons is enhanced in the CB of CdS QDs, which translates to high EQEs. In the wavelength range of 600−1000 nm, the EQE values are zero for the TiO_2/CdS and TiO_2/CdS/Cu NP based cells. However, the EQE performance of the TiO_2/CdS/Cu NN based cell is markedly different in the 600−1000 nm wavelength span; it varies from 1.5% to 4% and shows a weak maximum at about 924 nm. This response unambiguously shows that the far-field scattering effect of Cu NNs contributes to increased light absorption at energies below the band gap of the CdS QDs. The exact mechanism of this behavior is not clear, but since the absorption due to the longitudinal mode of Cu NNs is the noticeable distinguishing feature, the anomalous EQE response can be attributed to the same. The trend of IQE variation with wavelength is almost similar to that of EQE variation for all three cells. The magnitudes of IQE are slightly greater than those of the corresponding EQEs, which is natural, because the reflection and transmission losses are now accounted for. The highest IQE is about 66% for the TiO_2/CdS/Cu NN based cell, followed by 50% and 43% for the TiO_2/CdS and TiO_2/CdS/Cu NP based cells. The maximum IQE is about 5% in the 600−1000 nm wavelength region for the TiO_2/CdS/Cu NN based cell, which is in line with the corresponding EQE variation. In the past, Choi et al. measured the incident photon-to-current conversion efficiency (IPCE) values at 450 nm of CdS, CdS/JK-216, and CdS/Al_2O_3/JK-216, and they were found to be 47%, 50%, and 67%, respectively.[30] Kim et al. showed the prevention of back electron transfer by use of a $TiCl_4$ coating, and the IPCE for the TiO_2/CdS system was about 50% in the 400−500 nm solar region.[31] Wu et al. constructed a TiO_2−Au−CdS sandwich-like photoanode, and showed the plasmonic enhancement induced by Au NPs in the TiO_2−CdS system; a J_{SC} of 4 mA cm^{-2} was achieved.[32]

CONCLUSIONS

The light-scattering effects of low-cost Cu nanostructures permit energy-harvesting possibilities which are impossible with pristine quantum dots. We demonstrated this for the first time by tapping the light-scattering advantages offered by Cu nanostructures (NPs and NNs), and in particular Cu NNs. By incorporating them into a TiO_2/CdS assembly by electrophoresis, a significant increase in the light absorption capability of TiO_2/CdS was realized. Unlike Cu NPs, which due to size constraints increase light absorption only in the visible region, Cu NNs, owing to their longitudinal size effects, enhance light absorption in the NIR region as well, which translates to a remarkably enhanced PCE of 4.36% (best cell) for the corresponding QDSC. The ability of Cu NNs to accept electrons via Fermi level equilibration from CdS QDs, due to an electrical conductivity 4 times greater than that of Cu NPs, and their role in shifting the Fermi level of the TiO_2/CdS/Cu NN electrode to more positive potentials (with reference to the *vacuum* energy level) relative to the TiO_2/CdS and TiO_2/CdS/Cu NP electrodes were confirmed by fluorescence quenching, excited electron lifetime, and KPFM data analysis. Cu NNs endow the TiO_2/CdS photoanode with a transformative solar cell performance, as a PCE higher by 56.8% and 32.1% is achieved for the TiO_2/CdS/Cu NN based QDSC. We further show the use of a carbon fabric as a low-cost, directly usable, and equally performing attractive counter electrode alternative to traditional counter electrodes, which therefore can be applied to a gamut of solution-processed solar cells. The solar cell based on the TiO_2/CdS/Cu NN photoanode exhibited an EQE of 58% in the photopic region, and the ability of Cu NNs to increase the EQE in the NIR region, a phenomenon that is not possible in the cells based on the TiO_2/CdS and TiO_2/CdS/Cu NP electrodes, was also shown. This study involving the use of Cu NNs in QD-sensitized titania opens up a vista of opportunities for amplifying the solar cell response of different solution-processed solar cells by using inexpensive, earth-abundant Cu nanostructures.

ASSOCIATED CONTENT

Supporting Information

XRD patterns of Cu products, SEM images of TiO_2/CdS, KPFM of TiO_2, $J-V$ characteristics of cells with different electrolytes, $I-V$ plot of the carbon fabric, and tables of solar cell parameters for cells with different electrolytes, in terms of standard deviation, and corresponding to cell stability. The Supporting Information is available free of charge on the ACS Publications website at DOI: 10.1021/acsami.5b01175.

AUTHOR INFORMATION

Corresponding Author

*E-mail: mdeepa@iith.ac.in. Phone: +91-40-23016024. Fax: +91-40-23016003.

Notes

The authors declare no competing financial interest.

ACKNOWLEDGMENTS

Financial support from the Solar Energy Research Initiative—Department of Science & Technology (Grant DST/TM/SERI/2K12-11(G)) is gratefully acknowledged. P.N.K. thanks the

DOI: 10.1021/acsami.5b01175
ACS Appl. Mater. Interfaces 2015, 7, 13303−13313

University Grants Commission (UGC) for a grant for a junior research fellowship.

REFERENCES

(1) Hyunbong, C.; Wei, T. C.; Kamat, P. V. Know Thy Nano Neighbor. Plasmonic versus Electron Charging Effects of Metal Nanoparticles in Dye-Sensitized Solar Cells. *ACS Nano* **2012**, *6*, 4418−4427.

(2) Long, R.; Prezhdo, O. V. Instantaneous Generation of Charge-Separated State on TiO_2 Surface Sensitized with Plasmonic Nanoparticles. *J. Am. Chem. Soc.* **2014**, *136*, 4343−4354.

(3) Qi, J.; Dang, X.; Hammond, P. T.; M. Belcher, A. Highly Efficient Plasmon-Enhanced Dye-Sensitized Solar Cells through Metal@Oxide Core-Shell Nanostucture. *ACS Nano* **2011**, *5*, 7108−7116.

(4) Sheehan, W.; Noh, H.; Brudvig, G. W.; Cao, H.; Schmuttenmaer, C. A. Plasmonic Enhancement of Dye-Sensitized Solar Cells Using Core−Shell−Shell Nanostructures. *J. Phys. Chem. C* **2013**, *117*, 927−934.

(5) Zhang, W.; Saliba, M.; Stranks, S. D.; Sun, Y.; Shi, X.; Wiesner, U.; Snaith, H. J. Enhancement of Perovskite-Based Solar Cells Employing Core−Shell Metal Nanoparticles. *Nano Lett.* **2013**, *13*, 4505−4510.

(6) Zarick, H. F.; Hurd, O.; Webb, J. A.; Hungerford, C.; Erwin, W. R.; Bardhan, R. Enhanced Efficiency in Dye-Sensitized Solar Cells with Shape-Controlled Plasmonic Nanostructures. *ACS Photonics* **2014**, *1*, 806−811.

(7) Gangishetty, M. K.; Lee, K. E.; Scott, R. W. J.; Kelly, T. L. Plasmonic Enhancement of Dye Sensitized Solar Cells in the Red-to-Near-Infrared Region Using Triangular Core-Shell $Ag@SiO_2$ Nanoparticles. *ACS Appl. Mater. Interfaces* **2013**, *5*, 11044−11051.

(8) Li, H.; Yuan, K.; Zhang, Y.; Wang, J. Synthesis of Au-SiO_2 Asymmetric Clusters and Their Application in ZnO Nanosheet-Based Dye-Sensitized Solar Cells. *ACS Appl. Mater. Interfaces* **2013**, *5*, 5601−5608.

(9) Kumar, P. N.; Narayanan, R.; Deepa, M.; Srivastava, A. K. Au@Poly(acrylic acid) Plasmons and C_{60} Improve the Light Harvesting Capability of a TiO_2/CdS/CdSeS Photoanode. *J. Mater. Chem. A* **2014**, *2*, 9771−9783.

(10) Kumar, P. N.; Mandal, S.; Deepa, M.; Srivastava, A. K.; Joshi, A. G. Functionalized Graphite Platelets and Lead Sulfide Quantum Dots Enhance Solar Conversion Capability of a Titanium Dioxide/Cadmium Sulfide Assembly. *J. Phys. Chem. C* **2014**, *118*, 18924−18937.

(11) Parsi Benehkohal, N.; González-Pedro, V.; Boix, P. P.; Chavhan, S.; Tena-Zaera, R.; Demopoulos, G. P.; Mora-Seró, I. Colloidal PbS and PbSeS Quantum Dot Sensitized Solar Cells Prepared by Electrophoretic Deposition. *J. Phys. Chem. C* **2012**, *116*, 16391−16397.

(12) Choi, H.; Radich, J. G.; Kamat, P. V. Sequentially Layered CdSe/CdS Nanowire Architecture for Improved Nanowire Solar Cell Performance. *J. Phys. Chem. C* **2014**, *118*, 206−213.

(13) Zhang, H.; Cheng, K.; Hou, Y. M.; Fang, Z.; Pan, Z. X.; Wu, W. J.; Hua, J. L.; Zhong, X. H. Efficient CdSe Quantum Dot-Sensitized Solar Cells Prepared by a Postsynthesis Assembly Approach. *Chem. Commun.* **2012**, *48*, 11235−11237.

(14) Hossain, M. A.; Jennings, J. R.; Shen, C.; Pan, J. H.; Koh, Z. Y.; Mathews, N.; Wang, Q. CdSe-Sensitized Mesoscopic TiO_2 Solar Cells Exhibiting >5% Efficiency: Redundancy of CdS Buffer Layer. *J. Mater. Chem.* **2012**, *22*, 16235−16242.

(15) Pan, Z.; Zhang, H.; Cheng, K.; Hou, Y.; Hua, J.; Zhong, X. Highly Efficient Inverted Type-I CdS/CdSe Core/Shell Structure QD-Sensitized Solar Cells. *ACS Nano* **2012**, *6*, 3982−3991.

(16) Yan, K.; Zhang, L.; Qiu, J.; Qiu, Y.; Zhu, Z.; Wang, J.; Yang, S. A Quasi-Quantum Well Sensitized Solar Cell with Accelerated Charge Separation and Collection. *J. Am. Chem. Soc.* **2013**, *135*, 9531−9539.

(17) Chang, Y.; Lye, M. L.; Zeng, H. C. Large-Scale Synthesis of High-Quality Ultralong Copper Nanowires. *Langmuir* **2005**, *21*, 3746−3748.

(18) Warren, S. C.; Thimsen, E. Plasmonic Solar Water Splitting. *Energy Environ. Sci.* **2012**, *5*, 5133.

(19) Warren, S. C.; Thimsen, E. Plasmonic Solar Water Splitting. *Energy Environ. Sci.* **2012**, *5*, 5133−5146.

(20) Kamat, P. V. Quantum Dot Solar Cells. The Next Big Thing in Photovoltaics. *J. Phys. Chem. Lett.* **2013**.

(21) Jakob, M.; Levanon, H.; Kamat, P. V. Charge Distribution between UV-Irradiated TiO_2 and Gold Nanoparticles: Determination of Shift in the Fermi Level. *Nano Lett.* **2003**, *3*, 353−358.

(22) Subramanian, V.; Wolf, E. E.; Kamat, P. V. Catalysis with TiO_2/Gold Nanocomposites. Effect of Metal Particle Size on the Fermi Level Equilibration. *J. Am. Chem. Soc.* **2004**, *126*, 4943−4950.

(23) Kamat, P. V. Quantum Dot Solar Cells. Semiconductor Nanocrystals as Light Harvesters. *J. Phys. Chem. C* **2008**, *112*, 18737−18753.

(24) Santra, P. K.; Kamat, P. V. Tandem-Layered Quantum Dot Solar Cells: Tuning the Photovoltaic Response with Luminescent Ternary Cadmium Chalcogenides. *J. Am. Chem. Soc.* **2013**, *135*, 877−885.

(25) Yin, Z.; Zhu, J.; He, Q.; Cao, X.; Tan, C.; Chen, H.; Yan, Q.; Zhang, H. Graphene-Based Materials for Solar Cell Applications. *Adv. Energy Mater.* **2014**, *4*, 1−19.

(26) Murakami, T. N.; Grätzel, M. Counter Electrodes for DSC: Application of Functional Materials as Catalysts. *Inorg. Chim. Acta* **2008**, *361*, 572−580.

(27) Chen, X.; Shen, S.; Guo, L.; Mao, S. S. Semiconductor-Based Photocatalytic Hydrogen Generation. *Chem. Rev.* **2010**, *110*, 6503−6570.

(28) Li, L.; Yang, X.; Gao, J.; Tian, H.; Zhao, J.; Hagfeldt, A.; Sun, L. Highly Efficient CdS Quantum Dot-Sensitized Solar Cells Based on a Modified Polysulfide Electrolyte. *J. Am. Chem. Soc.* **2011**, *133*, 8458−8460.

(29) Wang, Y.; Peng, N.; Li, H.; Bai, X. High-Efficiency CdS Quantum-Dots-Sensitized Solar Cells with Compressed Nanocrystalline TiO_2 Photoelectrodes. *J. Nanomater.* **2012**, 1−6.

(30) Sun, W. T.; Yu, Y.; Pan, H. Y.; Gao, X. F.; Chen, Q.; Peng, L. M. CdS Quantum Dots Sensitized TiO_2 Nanotube-Array Photoelectrodes. *J. Am. Chem. Soc.* **2008**, *130*, 1124−1125.

(31) Shen, Q.; Toyoda, T. Ultrafast Electron and Hole Dynamics in CdSe Quantum Dot Sensitized Solar Cells. *Sol. Cells—New Aspects Solutions* **2011**, 287−306.

(32) Shalom, M.; Albero, J.; Tachan, Z.; Martínez-Ferrero, E.; Zaban, A.; Palomares, E. Quantum Dot-Dye Bilayer-Sensitized Solar Cells: Breaking the Limits Imposed by the Low Absorbance of Dye Monolayers. *J. Phys. Chem. Lett.* **2010**, *1*, 1134−1138.

(33) Ehrler, B.; Musselman, K. P.; Böhm, M. L.; Morgenstern, F. S. F.; Vaynzof, Y.; Walker, B. J.; Macmanus-Driscoll, J. L.; Greenham, N. C. Preventing Interfacial Recombination in Colloidal Quantum Dot Solar Cells by Doping the Metal Oxide. *ACS Nano* **2013**, *7*, 4210−4220.

(34) Shalom, M.; Tachan, Z.; Bouhadana, Y.; Barad, H. N.; Zaban, A. Illumination Intensity-Dependent Electronic Properties in Quantum Dot Sensitized Solar Cells. *J. Phys. Chem. Lett.* **2011**, *2*, 1998−2003.

DOI: 10.1021/acsami.5b01175
ACS Appl. Mater. Interfaces 2015, 7, 13303−13313